Robot Calibration combining Kinematic Model and Neural Network for enhanced Positioning and Orientation Accuracy ⋆

Stefan Gadringer * Hubert Gattringer * Andreas Müller * Ronald Naderer **

* *Institute of Robotics, Johannes Kepler University Linz, Altenbergerstraße 69, 4040 Linz, Austria (e-mail: {stefan.gadringer, hubert.gattringer, a.mueller}@jku.at).*
** *FerRobotics Compliant Robot Technology GmbH, Altenbergerstraße 69, 4040 Linz, Austria (e-mail: ronald.naderer@ferrobotics.at)*

Abstract: Traditionally, the calibration of robots is pursued either using model-based or model-free methods. Only a few attempts to combine both approaches were reported, particularly the combination of geometric calibration and artificial neural network (ANN). The latter was mostly used to compensate the positioning error, however. This paper introduces an ANN for compensation of residual positioning as well as orientation error. Moreover, the ANN compensation can be applied with or without prior geometric calibration. An automatic measurement procedure was developed and nearly 14 000 robot poses were measured using a laser tracker. Five-fold cross validation on the training data was applied to find the best parameters of the ANN. These tests indicate that better accuracy is achievable by combining geometric calibration and ANN. Applying this combination on the test data reduced the maximum/average position error to 6.28 %/4.26 % and the maximum/average orientation error to 7.41 %/3.34 % of the original values (obtained without calibration).

Keywords: Robot calibration, model identification, neural networks, positioning accuracy, orientation accuracy, robot kinematics, industrial robots

1. INTRODUCTION

Modern industrial robots are more and more used for automated manufacturing tasks like grinding, milling, or measuring. Thus, high positioning and orientation accuracy is essential and can only be achieved by robot calibration. According to Elatta et al. (2004), calibration methods are typically classified as model-based or model-free approaches.

Model-based approaches take error sources in the robot model into account. As mentioned in Roth et al. (1987), many researcher considered deviations in the geometric parameters of the kinematic model, which is also known as geometric calibration. Neubauer et al. (2015) additionally compensated non-geometric error sources like joint and drive stiffness to achieve an improved robot accuracy. While this parametric calibration procedure works very well, at the same time, requires some effort in robot modelling.

Model-free, or rather non-parametric approaches do not rely on modelling of error sources. Instead, error compensation is pursued directly on measurement. Bai (2007) used a 3D grid to divide the robot workspace in small discrete areas and measured the end effector error at all grid points. The error compensation of a distinct robot pose was achieved by fuzzy interpolation of the measured errors of the surrounding grid points. Meggiolaro et al. (2005) used polynomial approximations to consider errors due to geometric and elastic deformation of a patient positioning system.

Some preliminary work of combining the advantages of parametric and non-parametric approaches was carried out several years ago by Zhong et al. (1996) who applied an artificial neural network (ANN) for inverse calibration compensation. However, the training data was inaccurate due to the usage of nominal inverse kinematics. Nguyen et al. (2015) geometrically calibrated a robot and further used an ANN with the robot joint angles as inputs to compensate residual positioning errors due to unmodelled error sources, which represents a forward calibration compensation procedure. Zhao et al. (2019) revised this approach and used many more measurements to compensate the non-linear residual positioning errors even better. However, the orientation error was not considered and just a limited workspace was used.

The aim of this paper is to amend the approach of Zhao et al. (2019) and extend it with orientation information for combined compensation of positioning and orientation error within the whole workspace. This paper also addresses the question as to what extent geometric calibration prior

⋆ This work has been supported by the "LCM - K2 Center for Symbiotic Mechatronics" within the framework of the Austrian COMET-K2 program.

Preprints of the 21st IFAC World Congress (Virtual)
Berlin, Germany, July 12-17, 2020

to ANN error compensation further improves robot accuracy.

2. ROBOT KINEMATICS

2.1 Forward Kinematics

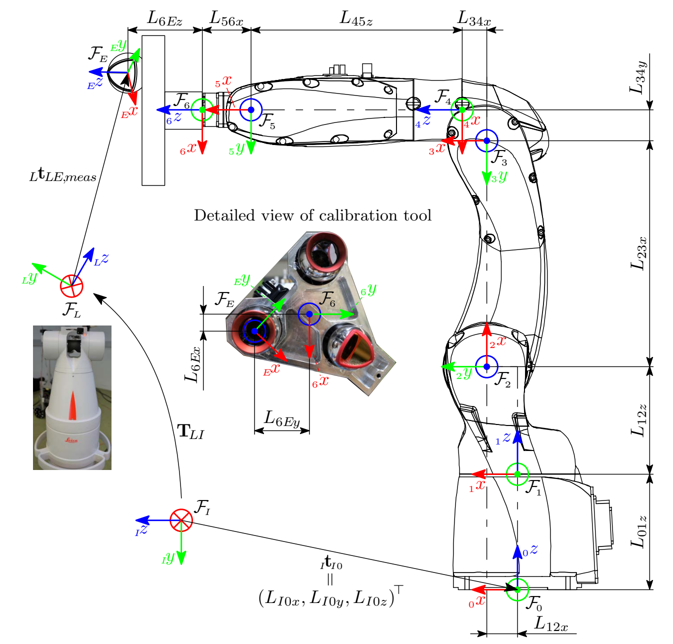

Fig. 1. COMAU R5 robot with defined frames

Figure 1 shows the 6-DOF-robot COMAU Racer5-0.80 with joint angles q_1 to q_6 and corresponding body-fixed frames $\mathcal{F}_1$ to $\mathcal{F}_6$. The z-axes of frames $\mathcal{F}_1$ to $\mathcal{F}_6$ are defined by the rotation axes, respectively. The inertial frame $\mathcal{F}_I$ serves as a point of reference for the application. The frame at the end effector (calibration tool) is denoted by $\mathcal{F}_E$. The position of the end effector is measured with a Leica laser tracker with reference frame $\mathcal{F}_L$.

For the modelling of the kinematics, homogeneous transformation matrices are used and the notation is as follows. The relative configuration of frames $\mathcal{F}_B$ and $\mathcal{F}_I$ is described by the homogeneous transformation matrix

$$\mathbf{T}_{IB} = \begin{bmatrix} \mathbf{R}_{IB} & {}_I\mathbf{t}_{IB} \\ 0 & 1 \end{bmatrix}, \tag{1}$$

where ${}_I\mathbf{t}_{IB} \in \mathbb{R}^3$ is the coordinate vector of the origin of $\mathcal{F}_B$, measured and resolved in $\mathcal{F}_I$ and $\mathbf{R}_{IB} \in \mathrm{SO}(3)$ represents the orientation of frame $\mathcal{F}_B$ in $\mathcal{F}_I$. Rotation matrices are parameterized in terms of Cardan angles ($x-y-z$ rotations), denoted as $\mathbf{R}(\alpha, \beta, \gamma)$.

Table 1 summarizes the nominal translation and orientation of the zero reference configuration of the COMAU Racer5-0.80 using nominal parameters $\mathbf{p}_{geo}$. For example, the nominal coordinate transformation from $\mathcal{F}_0$ to $\mathcal{F}_I$ is determined by the rotation matrix $\overline{\mathbf{R}}_{I0}(\pi/2,\ 0,\ \pi/2)$ and the translation vector ${}_I\overline{\mathbf{t}}_{I0} = (L_{I0x}, L_{I0y}, L_{I0z})^\top$, which leads to the homogeneous transformation matrix

$$\overline{\mathbf{T}}_{I0} = \begin{bmatrix} \overline{\mathbf{R}}_{I0} & {}_I\overline{\mathbf{t}}_{I0} \\ 0 & 1 \end{bmatrix}. \tag{2}$$

Table 1. Transformations with its nominal geometric parameters and joint coordinates

$\mathbf{T}$	$\mathbf{p}_{geo}$: $\overline{\varphi}_{Cardan}$ in rad	$\mathbf{p}_{geo}$: $\overline{\mathbf{t}}$ in m	$\mathbf{q}$	$\mathbf{T}$	$\mathbf{p}_{geo}$: $\overline{\varphi}_{Cardan}$ in rad	$\mathbf{p}_{geo}$: $\overline{\mathbf{t}}$ in m	$\mathbf{q}$
$\mathbf{T}_{I0}$	$\pi/2$ 0 $\pi/2$	L_{I0x} L_{I0y} L_{I0z}		$\mathbf{T}_{34}$	$\pi/2$ $\pi/2$ 0	L_{34x} L_{34y} 0	q_4
$\mathbf{T}_{01}$	0 0 0	0 0 L_{01z}	q_1	$\mathbf{T}_{45}$	$-\pi/2$ 0 $-\pi/2$	0 0 L_{45z}	q_5
$\mathbf{T}_{12}$	$-\pi/2$ 0 $-\pi/2$	L_{12x} 0 L_{12z}	q_2	$\mathbf{T}_{56}$	$\pi/2$ $\pi/2$ 0	L_{56x} 0 0	q_6
$\mathbf{T}_{23}$	0 0 $\pi/2$	L_{23x} 0 0	q_3	$\mathbf{T}_{6E}$	0 0 $\pi/4$	L_{6Ex} L_{6Ey} L_{6Ez}	

The transformation matrix for adjacent frames is

$$\mathbf{T}_{i-1,i} = \begin{bmatrix} \overline{\mathbf{R}}_{i-1,i}\,\mathbf{R}_z(q_i) & {}_{i-1}\overline{\mathbf{t}}_{i-1,i} \\ 0 & 1 \end{bmatrix} \tag{3}$$

with $i = 1 \ldots 6$ and the one for the end effector is

$$\mathbf{T}_{6E} = \begin{bmatrix} \overline{\mathbf{R}}_{6E} & {}_6\overline{\mathbf{t}}_{6E} \\ 0 & 1 \end{bmatrix}. \tag{4}$$

Finally, this leads to the overall transformation matrix from $\mathcal{F}_E$ to $\mathcal{F}_I$

$$\mathbf{T}_{IE} = \mathbf{T}_{I0}\,\mathbf{T}_{01}\,\mathbf{T}_{12}\,\mathbf{T}_{23}\,\mathbf{T}_{34}\,\mathbf{T}_{45}\,\mathbf{T}_{56}\,\mathbf{T}_{6E}. \tag{5}$$

2.2 Geometric Error Modelling

The kinematic model with geometric errors accounts for $n_e = 48$ error parameters, as shown in Table 2. The vector of geometric error parameters $\mathbf{p}_e \in \mathbb{R}^{n_e}$ consists of the parameter vector $\mathbf{p}_L$ due to length deviations as well as the parameter vector $\mathbf{p}_R$ due to inaccurate zero positions and axes misalignment.

Table 2. Geometric error parameters

$\hat{\mathbf{T}}$	$\mathbf{p}_e$: $\mathbf{p}_L$ in m	$\mathbf{p}_e$: $\mathbf{p}_R$ in rad	$\hat{\mathbf{T}}$	$\mathbf{p}_e$: $\mathbf{p}_L$ in m	$\mathbf{p}_e$: $\mathbf{p}_R$ in rad
$\hat{\mathbf{T}}_{I0}$	$p_{L\,I0x}$ $p_{L\,I0y}$ $p_{L\,I0z}$	$p_{R\,I0x}$ $p_{R\,I0y}$ $p_{R\,I0z}$	$\hat{\mathbf{T}}_{34}$	$p_{L\,34x}$ $p_{L\,34y}$ $p_{L\,34z}$	$p_{R\,34x}$ $p_{R\,34y}$ p_{q4}
$\hat{\mathbf{T}}_{01}$	$p_{L\,01x}$ $p_{L\,01y}$ $p_{L\,01z}$	$p_{R\,01x}$ $p_{R\,01y}$ p_{q1}	$\hat{\mathbf{T}}_{45}$	$p_{L\,45x}$ $p_{L\,45y}$ $p_{L\,45z}$	$p_{R\,45x}$ $p_{R\,45y}$ p_{q5}
$\hat{\mathbf{T}}_{12}$	$p_{L\,12x}$ $p_{L\,12y}$ $p_{L\,12z}$	$p_{R\,12x}$ $p_{R\,12y}$ p_{q2}	$\hat{\mathbf{T}}_{56}$	$p_{L\,56x}$ $p_{L\,56y}$ $p_{L\,56z}$	$p_{R\,56x}$ $p_{R\,56y}$ p_{q6}
$\hat{\mathbf{T}}_{23}$	$p_{L\,23x}$ $p_{L\,23y}$ $p_{L\,23z}$	$p_{R\,23x}$ $p_{R\,23y}$ p_{q3}	$\hat{\mathbf{T}}_{6E}$	$p_{L\,6Ex}$ $p_{L\,6Ey}$ $p_{L\,6Ez}$	$p_{R\,6Ex}$ $p_{R\,6Ey}$ $p_{R\,6Ez}$

Considering these error parameters, the corresponding parameter dependent rotation matrices are

$$\hat{\mathbf{R}}_{I0} = \overline{\mathbf{R}}_{I0}\,\mathbf{R}(p_{R\,I0x}, p_{R\,I0y}, p_{R\,I0z}), \tag{6}$$

$$\hat{\mathbf{R}}_{i-1,i} = \overline{\mathbf{R}}_{i-1,i}\,\mathbf{R}(p_{R\,i-1,ix}, p_{R\,i-1,iy}, q_i + p_{q,i}), \tag{7}$$

$$\hat{\mathbf{R}}_{6E} = \overline{\mathbf{R}}_{6E}\,\mathbf{R}(p_{R\,6Ex}, p_{R\,6Ey}, p_{R\,6Ez}), \tag{8}$$

and the translation vectors are

$$ {}_I\hat{\mathbf{t}}_{I0} = {}_I\bar{\mathbf{t}}_{I0} + (p_{L\,I0x}, p_{L\,I0y}, p_{L\,I0z})^\top , \tag{9}$$
$$ {}_{i-1}\hat{\mathbf{t}}_{i-1,i} = {}_{i-1}\bar{\mathbf{t}}_{i-1,i} + (p_{L\,i-1,ix}, p_{L\,i-1,iy}, p_{L\,i-1,iz})^\top , \tag{10}$$
$$ {}_6\hat{\mathbf{t}}_{6E} = {}_6\bar{\mathbf{t}}_{6E} + (p_{L\,6Ex}, p_{L\,6Ey}, p_{L\,6Ez})^\top \tag{11}$$

where $i = 1 \ldots 6$. Hence, (5) changes to

$$\begin{aligned} \hat{\mathbf{T}}_{IE} &= \hat{\mathbf{T}}_{I0}\,\hat{\mathbf{T}}_{01}\,\hat{\mathbf{T}}_{12}\,\hat{\mathbf{T}}_{23}\,\hat{\mathbf{T}}_{34}\,\hat{\mathbf{T}}_{45}\,\hat{\mathbf{T}}_{56}\,\hat{\mathbf{T}}_{6E} \\ &= \begin{bmatrix} \hat{\mathbf{R}}_{IE} & {}_I\hat{\mathbf{t}}_{IE} \\ 0 & 1 \end{bmatrix}, \end{aligned} \tag{12}$$

where ${}_I\hat{\mathbf{t}}_{IE}$ is the position of the end effector, represented in $\mathcal{F}_I$. The rotation matrix $\hat{\mathbf{R}}_{IE}$ describes the orientation of $\mathcal{F}_E$ relative to $\mathcal{F}_I$.

2.3 Elimination of Linear Dependent Parameters

Considering position and orientation measurement, the end effector error $\Delta\mathbf{z} \in \mathbb{R}^6$ is defined as

$$\Delta\mathbf{z} = \begin{pmatrix} \Delta_I\mathbf{t}_{IE} \\ \Delta\varphi_{IE} \end{pmatrix} \tag{13}$$

with positioning error $\Delta_I\mathbf{t}_{IE} \in \mathbb{R}^3$ and orientation error $\Delta\varphi_{IE} \in \mathbb{R}^3$. Therein $\Delta\varphi_{IE}$ is proportional to the rotation axis that can be associated to the relative rotation (see Axis–Angle representation of Shuster (1993)).

Setting (13) to zero, i.e. $\Delta\mathbf{z} = \mathbf{0}$, provides six independent equations and leads to a non-linear optimization problem (root-finding) to find the geometric error parameters $\mathbf{p}_e$. This problem can be solved iteratively using a Taylor series of $\Delta\mathbf{z} = \Delta\mathbf{z}(\mathbf{z}_{meas}, \mathbf{q}, \mathbf{p}_e)$ at the start parameters $\mathbf{p}_e^{(0)}$, i.e.

$$\Delta\mathbf{z}(\mathbf{z}_{meas,j}, \mathbf{q}_j, \mathbf{p}_e^{(0)}) + \underbrace{\left.\frac{\partial\Delta\mathbf{z}}{\partial\mathbf{p}_e}\right|_{\mathbf{p}_e^{(0)}}}_{\mathbf{\Theta}_j} \Delta\mathbf{p}_e + \ldots = \mathbf{0} \tag{14}$$

or after evaluating (14) with $j = 1 \ldots m$ measurements

$$\underbrace{\begin{pmatrix} \Delta\mathbf{z}(\mathbf{z}_{meas,1}, \mathbf{q}_1, \mathbf{p}_e^{(0)}) \\ \vdots \\ \Delta\mathbf{z}(\mathbf{z}_{meas,m}, \mathbf{q}_m, \mathbf{p}_e^{(0)}) \end{pmatrix}}_{\mathbf{Q}} + \underbrace{\begin{pmatrix} \mathbf{\Theta}_1 \\ \vdots \\ \mathbf{\Theta}_m \end{pmatrix}}_{\mathbf{\Theta}} \Delta\mathbf{p}_e = \mathbf{0}. \tag{15}$$

Using position and orientation measurement for the geometric calibration leads to the regressor matrix $\mathbf{\Theta} \in \mathbb{R}^{n,n_e}$ with $n = 6m$ rows for m measurements. Not all of the n_e parameters deviations $\Delta\mathbf{p}_e \in \mathbb{R}^{n_e}$ are independent. Therefore, s linear dependent columns of $\mathbf{\Theta}$ are eliminated via a QR Decomposition $\mathbf{\Theta} = \hat{\mathbf{Q}}\,\hat{\mathbf{R}}$. This determines the identifiable geometric error parameter vector $\overline{\mathbf{p}}_e \in \mathbb{R}^{\overline{n}_e = n_e - s}$, which is also called base parameter vector. Using nominal forward kinematics with random joint angles instead of real measurements and following the procedure of Khalil and Gautier (1991), yields

$$\overline{\mathbf{Q}} + \overline{\mathbf{\Theta}}\,\Delta\overline{\mathbf{p}}_e = \mathbf{0} \tag{16}$$

with regressor matrix $\overline{\mathbf{\Theta}} \in \mathbb{R}^{6m,\overline{n}_e}$, parameters deviation vector $\Delta\overline{\mathbf{p}}_e \in \mathbb{R}^{\overline{n}_e}$ and $\overline{\mathbf{Q}} \in \mathbb{R}^{6m,1}$, which is a reordered version of $\mathbf{Q}$ after doing the same permutation as used for $\overline{\mathbf{\Theta}}$. The $\overline{n}_e = 30$ determined base parameters are given in Table 3.

3. MEASUREMENT PROCEDURE

As stated in Zhao et al. (2019), an ANN needs a large amount of training poses to guarantee successful modelling of the residual end effector error. The developed automatic measurement procedure consists of four stages: robot pose selection, suitability check, trajectory planning between poses and automatic measurement using laser tracker.

Table 3. Base parameters of COMAU R5

#	**Identifiable Parameters**		
1	$p_{L\,I0x} - p_{L\,01y} - 0.189\,p_{R\,01x}$		
2	$p_{L\,I0y} - p_{L\,01z} - p_{L\,12z}$		
3	$p_{L\,I0z} + p_{L\,01x} - 0.189\,p_{R\,01y}$		
4	$p_{L\,12x}$		
5	$p_{L\,12y} + p_{L\,23z} + p_{L\,34z} - 0.050\,p_{R\,12x}$		
6	$p_{L\,23x}$		
7	$p_{L\,23y} - 0.370\,p_{q3} - 0.370\,p_{R\,34y}$		
8	$p_{L\,34x} + p_{L\,45z} - 0.050\,p_{R\,34y}$		
9	$p_{L\,34y} - 0.041\,p_{R\,34y}$	20	$p_{q6} + p_{R\,6Ez}$
10	$p_{L\,45x}$	21	$p_{R\,I0x} + p_{R\,01x}$
11	$p_{L\,45y} + p_{L\,56z}$	22	$p_{R\,I0y} + p_{R\,01y}$
12	$p_{L\,56x} + p_{L\,6Ez}$	23	$p_{R\,12y}$
13	$p_{L\,56y} - 0.080\,p_{R\,56y}$	24	$p_{R\,23x}$
14	$p_{L\,6Ex} - 0.040\,p_{R\,6Ez}$	25	$p_{R\,23y}$
15	$p_{L\,6Ey} - 0.016\,p_{R\,6Ez}$	26	$p_{R\,34x}$
16	$p_{q1} + p_{R\,I0z} + p_{R\,12x}$	27	$p_{R\,45y}$
17	$p_{q2} + p_{q3} + p_{R\,34y}$	28	$p_{R\,56x}$
18	$p_{q4} + p_{R\,45x}$	29	$p_{R\,6Ex}$
19	$p_{q5} + p_{R\,56y}$	30	$p_{R\,6Ey}$

The used laser tracker LTD 800 from Leica Geosystems has a resolution of 1 µm and an accuracy of ±25 µm. To be able to measure position and orientation at the same time, three spherically mounted retroreflectors (SMR) are used. Figure 1 shows the setup of SMRs involving two red ring reflectors (RRR) and one break resistant reflector (BRR). The whole calibration setup is shown in Fig. 2. Using the SMRs for the measurement of the centre and respective points on x and y-axes of $\mathcal{F}_I$, allows the determination of $\mathbf{T}_{LI}$, which is constant for a rigid calibration setup. However, it should be noted that the robot setup stands on slightly elastic ground, i.e. compliant wooden structure.

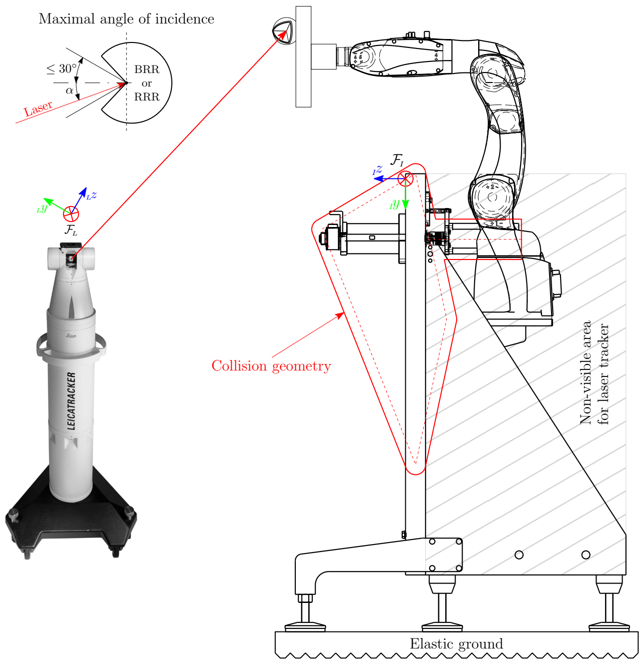

Fig. 2. Calibration setup with robot and laser tracker

The first stage of the measurement procedure requires to appropriately discretize the range of joint variables of the COMAU Racer5-0.80 with respective limits

$$\begin{aligned} -168^\circ \le q_1 \le 168^\circ \qquad -198^\circ \le q_4 \le 198^\circ \\ -83^\circ \le q_2 \le 133^\circ \qquad -98^\circ \le q_5 \le 98^\circ \\ -178^\circ \le q_3 \le 63^\circ \qquad -180^\circ \le q_6 \le 180^\circ. \end{aligned} \tag{17}$$

For example the first axis should be discretized with a higher resolution than the last one because a movement of q_1 has a higher impact on the end effector translation. Following this idea, the chosen discretization delivers joint values q_1 to q_6 every 19.80°, 21.60°, 24.10°, 28.30°, 32.70° and 36.00°, respectively, and results in 1 428 000 possible poses. These poses need to be checked for validity and suitability.

The suitability check involves three criteria. Firstly, the robot for selected joint coordinates must be outside the collision area, i.e. the minimal spatial distance between robot and collision objects must be greater than 3.50 cm.

Secondly, the calibration tool must be visible for the laser tracker, i.e. the calibration tool has to be above the wall as shown in Fig. 2. Finally, the opening angle α between laser and all three reflectors must be $|\alpha| \le 30^\circ$. To consider possible deviations of the reflector orientation and the shape of BRR, we decided to limit the allowed cone angles even more, i.e. $|\alpha_{RRR}| \le 26.50^\circ$ and $|\alpha_{BRR}| \le 20^\circ$. This results in 13 919 suitable poses for measurement of all three reflectors for position and orientation information.

The third stage of the measurement procedure is the trajectory planning between suitable poses. After separating the robot poses into poses in front of the wall and behind the wall, the trajectory is planned in joint coordinates. Simulating this trajectory and continuously calculating the minimal distance shows at which poses a collision between robot and environment would happen. After a few iterations of changing the order of critical poses, a valid trajectory without collision can be found.

The fourth stage is the automatic measurement itself. The laser tracker and the robot controller (B & R Automation PC) are able to communicate with each other using TCP/IP and allow to automatically measure the position of all three SMRs. At first the robot moves to a pose and gives a signal to the tracker after reach. Then the tracker measures all three reflectors and returns a signal after finish. This procedure is repeated until all poses are measured in the experiment. The measurement of all 13 919 poses took about 3.5 days and needed no supervision at all. Assuming known homogeneous transformation matrix $\mathbf{T}_{LI}$, the measurement of all three SMRs defines position ${}_I\mathbf{t}_{IE}$ and orientation via rotation matrix $\mathbf{R}_{IE}$.

4. GEOMETRIC CALIBRATION

Considering (16) and using well known method of least squares, the base parameters vector results in

$$\Delta\overline{\mathbf{p}}_e = -[\overline{\mathbf{\Theta}}^\top \overline{\mathbf{\Theta}}]^{-1} \overline{\mathbf{\Theta}}^\top \overline{\mathbf{Q}} \tag{18}$$

assuming enough measurements so that regressor matrix $\overline{\mathbf{\Theta}}$ has a full rank, i.e. $\mathrm{rank}(\overline{\mathbf{\Theta}}) = \overline{n}_e$. However, the full rank of $\overline{\mathbf{\Theta}}$ should be guaranteed due to the usage of regularization and randomly selected calibration poses.

The usage of Equ. (18) leads to the first solution $\overline{\mathbf{p}}_e^{(1)} = \overline{\mathbf{p}}_e^{(0)} + \Delta\overline{\mathbf{p}}_e$ of the geometric error parameters. For a more accurate solution of the non-linear model, more iterations are necessary, i.e.

$$\overline{\mathbf{p}}_e^{(n+1)} = \overline{\mathbf{p}}_e^{(n)} - [\overline{\mathbf{\Theta}}^\top \overline{\mathbf{\Theta}}]^{-1} \overline{\mathbf{\Theta}}^\top \overline{\mathbf{Q}}. \tag{19}$$

The parameters $\overline{\mathbf{p}}_e^{(0)} = \mathbf{0}$ can serve as the start parameters and the nominal parameters $\mathbf{p}_{geo}$ can be taken from publicly available CAD data. Table 4 summarizes the determined base parameters $\mathbf{p}_{base} = \overline{\mathbf{p}}_e^{(20)}$ using 220 random and independent from the previously derived 13 919 poses due to measurements for another research project.

Table 4. Determined geometric error parameters of COMAU Racer5-0.80

#	$\mathbf{p}_{base}$	Unit	#	$\mathbf{p}_{base}$	Unit
1	7.752×10^{-4}	m	16	8.150×10^{-4}	rad
2	2.343×10^{-3}	m	17	-1.054×10^{-4}	rad
3	-2.720×10^{-3}	m	18	3.050×10^{-3}	rad
4	-2.567×10^{-4}	m	19	-2.759×10^{-3}	rad
5	6.334×10^{-5}	m	20	1.279×10^{-2}	rad
6	1.676×10^{-3}	m	21	-8.877×10^{-4}	rad
7	5.611×10^{-4}	m	22	2.778×10^{-3}	rad
8	8.479×10^{-4}	m	23	-5.821×10^{-5}	rad
9	-3.293×10^{-4}	m	24	-1.393×10^{-4}	rad
10	8.669×10^{-5}	m	25	-2.455×10^{-4}	rad
11	-7.575×10^{-4}	m	26	2.380×10^{-4}	rad
12	-6.430×10^{-4}	m	27	-1.934×10^{-2}	rad
13	-2.026×10^{-5}	m	28	7.956×10^{-3}	rad
14	-1.524×10^{-3}	m	29	2.588×10^{-4}	rad
15	-1.639×10^{-3}	m	30	1.134×10^{-3}	rad

Figures 3 and 4 show the achieved reduction of positioning as well as orientation error. Yet unmodelled error sources, in particular the elastic ground of the robot setup, have a major negative influence on the robot accuracy.

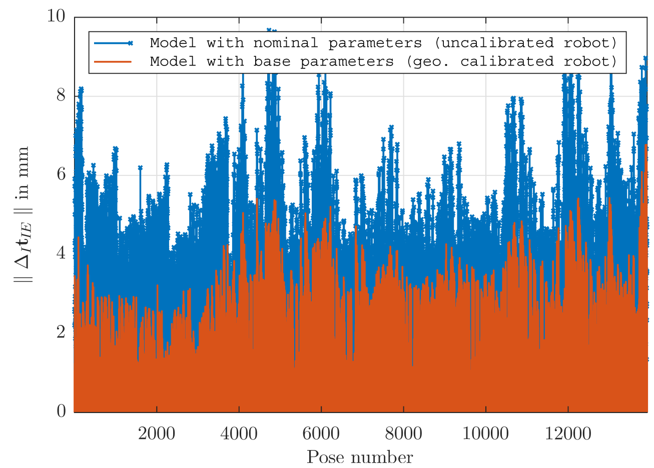

Fig. 3. Positioning error for the whole data

5. NEURAL NETWORK ERROR COMPENSATION

5.1 ANN Structure and Parameters

To further improve the positioning and orientation accuracy, an ANN with two hidden layers with respective hidden neurons N_1 and N_2 as well as an output layer with six neurons is considered. As common for regression,

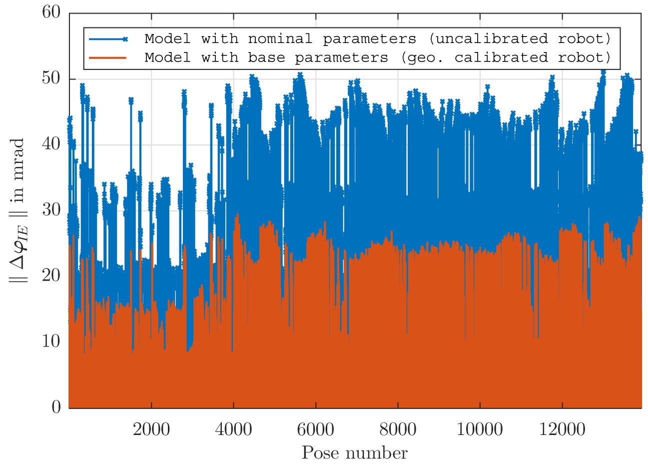

Fig. 4. Orientation error for the whole data

the two hidden layers use a hyperbolic tangent and the output layer a linear activation function. According to Zhao et al. (2019) and our own tests, more layers do not further improve the accuracy.

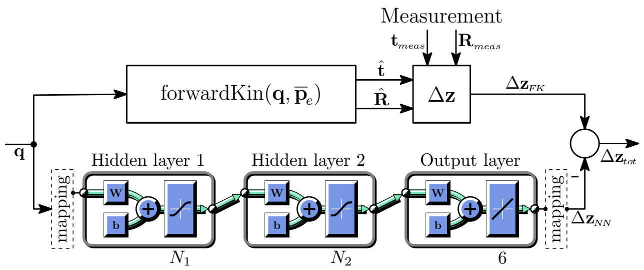

Fig. 5. Geometric error compensation with ANN

Figure 5 shows the structure of the ANN and thus how it is used to compensate the residual error $\Delta\mathbf{z}_{FK} \in \mathbb{R}^6$ to reduce error $\Delta\mathbf{z}_{tot} \in \mathbb{R}^6$. For training, i.e. supervised learning, the joint coordinates $\mathbf{q} \in \mathbb{R}^6$ serve as the input and the residual error $\Delta\mathbf{z}_{FK}$ using forward kinematics (with or without geometric error parameters) serve as the target. After training, the ANN should ideally be able to completely compensate the residual error for given joint coordinates.

As shown in Fig. 5, normalization/mapping is used for the inputs as well as targets/outputs of the ANN. Regarding to LeCun et al. (2012), normalization of the inputs potentially improves the convergence speed of an ANN during training. Additionally, mapping the joint coordinates with limits (17) to mean 0 and variance 1 assures the equal importance of all six inputs.

Likewise, normalization of the targets guarantees equal importance of the six outputs. Otherwise, the ANN might prefer to optimize the accuracy of an output element with higher range of target values compared to an element with smaller values using the mean squared error (MSE) as performance function for training. Considering the errors of Fig. 3 and 4, this would mean that the network would prefer to improve the orientation accuracy because the range of orientation errors is bigger than the range of positioning errors. To address this problem, we mapped the target data to mean 0 and variance 1 as done for the inputs.

5.2 Training

The networks are trained using batch learning and Bayesian regularization backpropagation, which is known to generate a network that generalizes well (see MacKay (1992) and Foresee and Hagan (1997)). This is achieved by minimization of squared errors and network weights instead of just the errors. So Bayesian regularization backpropagation successfully manages to avoid the overfitting problem even in the case when many hidden neurons or many training epochs are used.

To be able to verify the performance of a trained ANN, the recorded pose data is split into a training set with 11 136 poses (80 %) and a test set with 2783 poses (20 %). Applying five-fold cross validation on the training set helps to find the best number of hidden neurons (N_1, N_2). It should be noted, that mapping of inputs and outputs was applied separately to each training set.

Table 5 shows the cross validation results on the training set for the considered numbers of hidden neurons (16, 32 or 64 neurons per layer) using Bayesian regularization backpropagation (see MacKay (1992)) and 2048 training epochs. These results indicate, that the usage of geometric calibration indeed helps to improve the positioning and orientation accuracy even in the case of ANN error compensation. Furthermore, a higher number of hidden neurons might lead to even better results to the point where the ANN starts overfitting due to the usage of too many neurons. However, an ANN with more than (64, 32) hidden neurons was not tested due to limited time or rather computational power for training.

Table 5. Cross validation results on training data of tested ANNs

Hidden neurons	RMSE $\Delta\mathbf{z}_{tot}$	Max $\| \Delta_I\mathbf{t}_{IE} \|$ in mm	Max $\| \Delta\varphi_{IE} \|$ in mrad	$\overline{\mathbf{p}}_e$
(16, 16)	2.436	4.173	19.277	$\mathbf{0}$
(32, 16)	1.226	2.905	12.840	
(32, 32)	0.799	2.086	7.928	
(64, 32)	0.520	1.362	5.418	
(16, 16)	1.779	2.328	17.398	$\mathbf{p}_{base}$
(32, 16)	1.139	1.550	9.782	
(32, 32)	0.721	1.112	7.447	
(64, 32)	0.462	0.812	5.358	

The best results could be achieved with (64, 32) hidden neurons. Considering these parameters, we train two new ANNs (with and without prior geometric calibration) with new corresponding mappings using the whole training set to get the finally trained ANNs.

5.3 Test

The test set is used to check the performance of the two chosen ANNs on novel data. Figures 6 and 7 show the results, obtained with the proposed method. Compared to the uncalibrated robot, both ANNs compensate the positioning and orientation error very well.

Table 6 provides the statistical analysis of positioning and orientation error. The first column corresponds to the original results using kinematic model with nominal parameters. Column two shows the errors using geometric

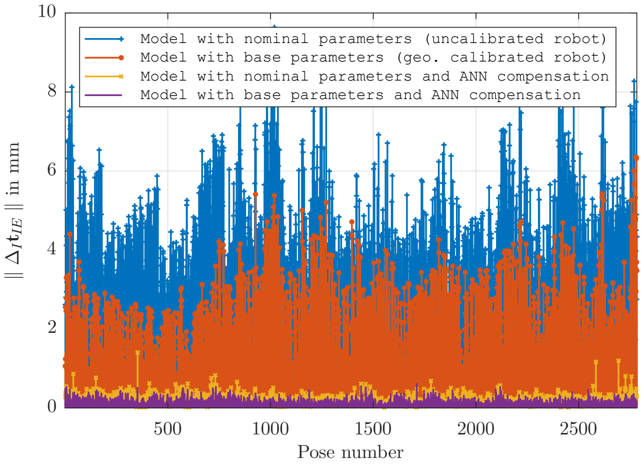

Fig. 6. Positioning error for the test data

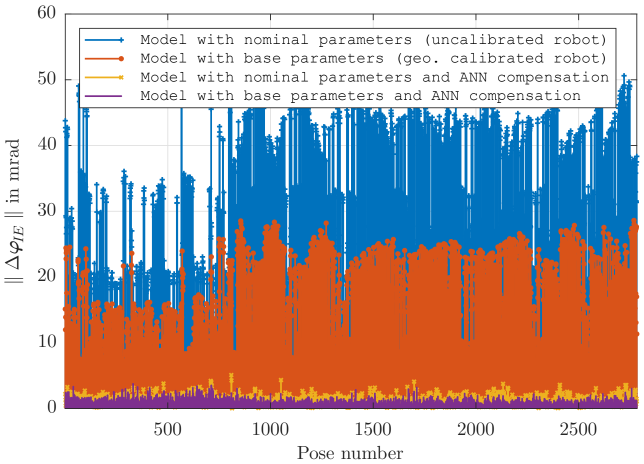

Fig. 7. Orientation error for the test data

calibration. The third column is associated with ANN $(64, 32)$ without prior geometric calibration. The best results are shown in the fourth column belonging to the combination of geometric calibration and ANN $(64, 32)$. For 2783 poses, the absolute positioning/orientation error is less than 0.605 mm/3.753 mrad and for 90 % of the poses (0.9-quantile $Q_{0.9}$) it is less than 0.258 mm/1.604 mrad.

Table 6. Positioning and orientation error for the test data

Error in mm or mrad	$\overline{\mathbf{p}}_e = \mathbf{0}$ no ANN	$\overline{\mathbf{p}}_e = \mathbf{p}_{base}$ no ANN	$\overline{\mathbf{p}}_e = \mathbf{0}$ ANN	$\overline{\mathbf{p}}_e = \mathbf{p}_{base}$ ANN
Max $\| \Delta_I \mathbf{t}_{IE} \|$	9.636	6.351	1.405	0.605
Mean $\| \Delta_I \mathbf{t}_{IE} \|$	3.522	1.844	0.192	0.150
$Q_{0.9}$ $\| \Delta_I \mathbf{t}_{IE} \|$	5.377	3.060	0.336	0.258
Max $\| \Delta\varphi_{IE} \|$	50.617	28.609	5.096	3.753
Mean $\| \Delta\varphi_{IE} \|$	28.063	15.191	1.076	0.938
$Q_{0.9}$ $\| \Delta\varphi_{IE} \|$	43.874	23.350	1.868	1.604

6. CONCLUSION

We proposed a combined model-based/model-free calibration method for an industrial robot and showed how we could use this model together with an ANN to achieve improved positioning and orientation accuracy in the whole workspace. The developed measurement procedure guaranteed the automatic measurement of 13 919 suitable robot poses without the requirement of human supervision. Combining geometric calibration and ANN leaded to a maximal positioning/orientation error of 0.605 mm/3.753 mrad, which is a reduction to 6.28 %/7.41 % of the error, obtained by the uncalibrated robot. Without prior geometric calibration, the ANN compensation resulted in similar but slightly higher errors. So the usage of a calibrated kinematic model indeed improved the accuracy. However, compared to the accuracy without any calibration, both ANN achieve a major improvement, which confirms the usefulness of our approach. Future work will involve tests of the developed calibration procedure also on other industrial robots to further prove the effectiveness. The usage of two separate networks for positioning and orientation error compensation might be another research topic.

REFERENCES

Bai, Y. (2007). On the comparison of model-based and modeless robotic calibration based on a fuzzy interpolation method. *The International Journal of Advanced Manufacturing Technology*, 31(11-12), 1243–1250.

Elatta, A., Gen, L.P., Zhi, F.L., Daoyuan, Y., and Fei, L. (2004). An overview of robot calibration. *Information Technology Journal*, 3(1), 74–78.

Foresee, F.D. and Hagan, M.T. (1997). Gauss-newton approximation to bayesian learning. In *Proceedings of International Conference on Neural Networks (ICNN'97)*, volume 3, 1930–1935.

Khalil, W. and Gautier, M. (1991). Calculation of the identifiable parameters for robots calibration. *IFAC Proceedings Volumes*, 24(3), 687–691.

LeCun, Y.A., Bottou, L., Orr, G.B., and Müller, K.R. (2012). Efficient backprop. In *Neural Networks: Tricks of the Trade*, 9–48. Springer.

MacKay, D.J. (1992). Bayesian interpolation. *Neural Computation*, 4(3), 415–447.

Meggiolaro, M.A., Dubowsky, S., and Mavroidis, C. (2005). Geometric and elastic error calibration of a high accuracy patient positioning system. *Mechanism and Machine Theory*, 40(4), 415–427.

Neubauer, M., Gattringer, H., Müller, A., Steinhauser, A., and Höbarth, W. (2015). A two-stage calibration method for industrial robots with joint and drive flexibilities. *Mechanical Sciences*, 6(2), 191–201.

Nguyen, H.N., Zhou, J., and Kang, H.J. (2015). A calibration method for enhancing robot accuracy through integration of an extended kalman filter algorithm and an artificial neural network. *Neurocomputing*, 151, 996–1005.

Roth, Z., Mooring, B., and Ravani, B. (1987). An overview of robot calibration. *IEEE Journal on Robotics and Automation*, 3(5), 377–385.

Shuster, M.D. (1993). A survey of attitude representations. *Journal of the Astronautical Sciences*, 41, 439–517.

Zhao, G., Zhang, P., Ma, G., and Xiao, W. (2019). System identification of the nonlinear residual errors of an industrial robot using massive measurements. *Robotics and Computer-Integrated Manufacturing*, 59, 104–114.

Zhong, X., Lewis, J., and N-Nagy, F.L. (1996). Inverse robot calibration using artificial neural networks. *Engineering Applications of Artificial Intelligence*, 9(1), 83–93.